Mechanics of Advanced Composite Structures

Journal homepage: https://macs.semnan.ac.ir/

Semnan University

ISSN: 2423-7043

Research Article

A Finite Element Formulation for Analyzing The Nonlinear Static Response of Bi-functionally Graded Microbeam Resting on Elastic Foundation Under Various Loads

Van-Chinh Nguyen, Trung Thanh Tran*

Faculty of Mechanical Engineering, Le Quy Don Technical University, Hanoi, Vietnam

ARTICLE INFO

Article history:

Received: 2023-10-19
Revised: 2024-03-22
Accepted: 2024-05-12

Keywords:

Microbeam;
2DFG;
Elastic foundation;
Nonlinear bending.

ABSTRACT

The main goal of this paper is to introduce a finite element formulation to investigate the nonlinear static response of the 2DFG-McrB resting on EF under four different loads. The governing equations are established using the principle of minimum potential energy, incorporating the RBT and geometric nonlinearity based on the von Kármán assumptions. A weak-form finite element method is developed and solved iteratively through the Newton-Raphson method. The proposed formulation is validated against benchmark results from the literature, demonstrating its accuracy and computational efficiency. Furthermore, a comprehensive parametric study is conducted to evaluate the effects of geometrical dimensions, material properties, foundation stiffness, length-scale parameters, and BCs on the nonlinear response of 2DFG-McrBs. The findings provide valuable insights for the design and analysis of McrBs in engineering applications and serve as a basis for future studies on advanced microstructures.

1. Introduction

McrBs play a crucial role in various small-scale systems and devices, particularly in MEMS and NEMS [1]. Owing to the complexity of loading conditions, McrBs in these applications often undergo significant deformations. Studying their behavior under such conditions is essential for the effective design and operation of microdevices. This has driven extensive research on the nonlinear static response of microstructures in general and McrBs in particular.

Extensive research has been conducted to predict the behavior of McrBs under various mechanical and electrical loading conditions. Early investigations were primarily based on classical beam theories, which do not adequately capture size-dependent effects. To address large rotations, many of these studies employed the von Kármán nonlinear assumption, analyzing McrB responses using methods such as the shooting method [2] and exact solutions [3, 4].

To overcome the limitations of classical beam theories in capturing size-dependent effects in microscale structures, several advanced

* **Corresponding author.**
E-mail address: tranthanh0212@gmail.com

Cite this article as:
Van Chinh Nguyen and Trung Thanh Tran, 2025. Title of article. *A finite element formulation for analyzing the nonlinear static response of bi-functionally graded microbeam resting on elastic foundation under various loads*, 12(1), pp. xx-xx
https://doi.org/10.22075/MACS.2024.39315.2050

continuum theories have been developed, including SGET [5, 6] and MCST [7]. These theories introduce length-scale parameters, enhancing the accuracy of modeling the mechanical behavior of McrBs. Over the past few years, numerous studies have utilized these advanced models to examine the impact of microscale effects on the mechanical behavior of McrBs. For instance, Mohammadi and Mahzoon [8] formulated the governing equations for post-buckling analysis of Euler-Bernoulli McrBs, incorporating size effects through both SGET and MCST. Xia et al. [9] developed a nonlinear beam model with a length-scale parameter, facilitating size-dependent analyses of static bending, post-critical behavior, and vibration in McrBs. Likewise, Asghari et al. [10] introduced a Timoshenko McrB model for nonlinear vibration and bending analysis, integrating size effects using MCST and SGET. Pham et al. [11] used a finite element modeling based on SGET and the refined HSDT to examine the dynamic instability of magnetically embedded FG porous nanobeams.

Furthermore, Akgoz and Civalek [12] explored the buckling behavior of McrBs under various BCs using EBBT and MCST. Ramezani [13] integrated the TBT with SGET to investigate the large-amplitude vibration of McrBs, emphasizing the crucial role of geometric nonlinearity in increasing beam frequencies. Ansari et al. [14] utilized DQM along with MCST to examine the bending, stability, and vibration of FG-McrBs, focusing on how frequencies and critical loads depend on the length-scale parameter. Additionally, Wang et al. [15] applied EBBT with MCST to study the nonlinear bending and thermal post-buckling behavior of McrBs, accounting for the influence of Poisson's ratio. Their analysis employed the shooting method in combination with the Newton iterative method to determine deflections and post-critical paths. Belabed et al. [16-20] used finite element procedure as a primary computational approach to investigate the mechanical behavior of various beam structures under different loading and BCs. Their comprehensive studies focused on analyzing key mechanical responses, including static bending, free vibration, and stability. The numerical results obtained from these analyses are presented in a thorough and systematic manner, providing valuable insights into the performance and reliability of beam systems in engineering applications. In addition, Meftah et al. [21] introduced FEM to describe the nonlinear modelling of masonry walls under in-plane loading. Tounsi et al. [22] analyzed the forced dynamical responses of FG porous beams using FEM.

Incorporating FGs into microstructures further enhances their potential by leveraging the materials' adaptability and multifunctionality. According to Benmesssaoud and Nasreddine [23], these materials are increasingly investigated for applications in micro-sensors, actuators, and flexible electronics. As a result, accurate and efficient computational modeling approaches have become essential [24, 25]. Using various shear deformation theories and MCST, researchers have extensively studied the linear static bending, vibration, and buckling behaviors of microbeams, microplates, and microshells. Notable contributions in this area include works by Şimşek et al. [26], Thai et al. [27], Deyhoriy-Semnani et al. [28]Sheikholeslami et al. [29], Akbas [30], Karamanli et al. [31, 32], Hu et al. [33] and Attia and Mohamed [34]. The nonlinear bending, vibration, and stability of microstructures have also been investigated by Shafiei et al. [35, 36] Attia and Mohamed [37]. Recently, Shenas et al. [38] analyzed the large amplitude vibration of pre-twisted FG-McrBs using the Chebyshev-Ritz method, and in [39] they employed the Ritz method to study the post-buckling thermal load–deflection path of rotating pre-twisted FG-McrBs in a thermal environment. Besides, Malekzadeh and Moradi [40] investigated large amplitude vibrational characteristics of variable-section thin beams with edge rotations restrained by elastic torsional springs and supported on a cubic non-linear EF using DQM. Pham et al. [41] used FEM to study free vibration of FG porous curved nanobeams resting on EF in hygro-thermo-magnetic environment.

In this study, we further investigate the size-dependent nonlinear static response of McrBs using a finite element procedure. A nonlinear beam element is developed based on RBT and MCST to derive the equilibrium equations. The model incorporates the von Kármán nonlinear assumption, with transverse shear rotation-rather than cross-sectional rotation-chosen as a variable to ensure a quadratic variation of moments along the beam length. Additionally, the nonlinear response of McrBs under various loading conditions is analyzed using the Newton-Raphson iterative method. This study also provides a comprehensive examination of the influence of geometrical parameters, material properties, foundation stiffness, length-scale parameters, and BCs on the nonlinear static response of 2DFG-McrB resting on an EF.

Beyond theoretical contributions, the findings of this study offer practical insights for the design and optimization of micro-scale devices, such as MEMS components, micro-sensors, actuators, etc. The proposed approach provides a valuable tool for engineers to predict structural performance more accurately, ensuring reliability and efficiency in real-world applications.

2. The 2DFG-McrB Resting on EF

Consider a 2DFG-McrB resting on an EF, having dimensions L, b, h along the x, y, and z axes, respectively, as shown in Fig. 1. The 2DFG-McrB includes two constituent phases: ceramic (denoted as c) and metal (denoted as m). The volume of these materials varies smoothly and continuously along the x and z directions following a power-law distribution. A two-parameter foundation model is employed, characterized by the spring stiffness k_W and the shear stiffness k_G. The beam is supported at both ends (at coordinates $x = 0$ and $x = L$) and is under a distributed load $q(x)$ along its length. Four types of load distributions are considered in this study: uniform load distribution (UL) $q(x) = q_0$, linear distribution load (LL) $q(x) = \frac{q_0 x}{L}$, parabolic distribution load (PL) $q(x) = q_0 \left(\frac{x}{L}\right)^2$, and sinusoidal distribution load (SL) $q(x) = q_0 \sin\frac{\pi x}{L}$ as shown in Fig. 2.

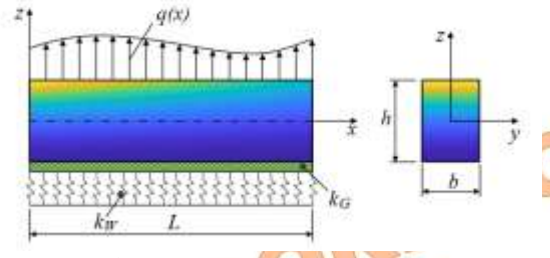

Fig. 1. The 2DFG-McrB model resting on EF

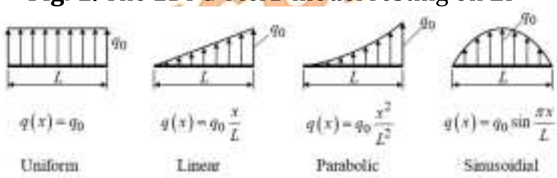

Fig. 2. Various types of loads

The mechanical properties of a 2DFG-McrB, including the elastic modulus $E(x, z)$, Poisson's ratio $\vartheta(x, z)$, and the length-scale parameter $\ell(x, z)$, vary continuously along both directions. These properties are collectively denoted as $\mathcal{F}(x, z)$ and are defined by the following expression:

$$\mathcal{F}(x, z) = V_c(x, z)\mathcal{F}_c + V_m(x, z)\mathcal{F}_m \tag{1}$$

Here, V_i represents the volume fraction of material i ($i = c, m$), which is defined by the following expression:

$$V_c(x, z) = \left(\frac{1}{2} + \frac{z}{h}\right)^{n_z} \left(1 - \frac{x}{2L}\right)^{n_x}, \quad V_m(x, z) = 1 - V_c(x, z) \tag{2}$$

where, n_x and n_z are non-negative values representing the material distribution exponents (power-law index) along the x and z directions, respectively.

Figure 3 demonstrates variations in the volume fractions of phases, as well as the variation in effective elastic modulus along the x and z directions. The material properties of the components are listed in Table 2 with $n_x = n_z = 2$.

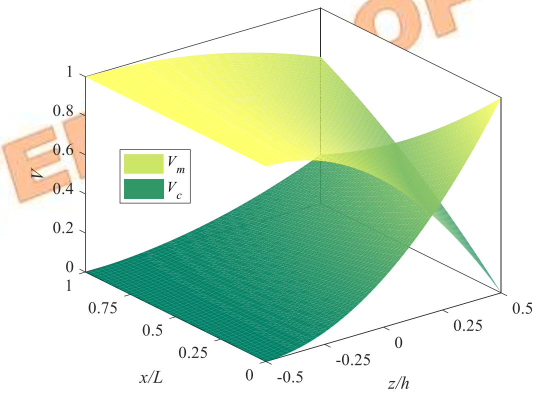

a) The volume fraction of phases

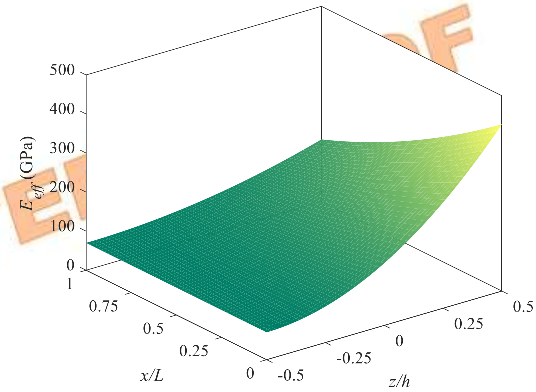

b) The effective elastic modulus

Fig 3. The variation in volume fraction of phases and effective elastic modulus of 2D-McrBs

3. Basis Formulations

The displacement field $\mathbf{u}$ in the beam includes two displacement components: the axial displacement $u(x, z)$ and the transverse displacement $w(x)$. It is defined by [42]:

$$\mathbf{u} = \begin{Bmatrix} u(x, z) \\ w(x) \end{Bmatrix} = \begin{Bmatrix} u_0 - z w_{b,x} - f(z) w_{s,x} \\ w_b + w_s \end{Bmatrix} \tag{3}$$

where u_0 is the axial displacement component on the midplane of beams, w_b and w_s are the transverse displacement components on the midplane are due to bending deformation and shear deformation, respectively. The derivative components are given by $w_{b,x} = \frac{\partial w_b}{\partial x}$, $w_{s,x} = \frac{\partial w_s}{\partial x}$ và $f(z) = \frac{4z^3}{3h^2}$.

The strain field $\boldsymbol{\varepsilon}$ is determined based on the displacement field using the Cauchy strain relations and the nonlinear von Kármán strain-displacement equations as follows:

$$\boldsymbol{\varepsilon} = \begin{Bmatrix} \varepsilon_x \\ \gamma_{xz} \end{Bmatrix}, \varepsilon_x = \frac{\partial u}{\partial x} + \frac{1}{2}\left(\frac{\partial w}{\partial x}\right)^2, \quad \gamma_{xz} = \frac{\partial u}{\partial z} + \frac{\partial w}{\partial x} \tag{4}$$

Substituting the displacement components u and w into the strain-displacement relations given in Eq. (4), we obtain:

$$\boldsymbol{\varepsilon} = \boldsymbol{\varepsilon}_L + \boldsymbol{\varepsilon}_{NL},$$

$$\boldsymbol{\varepsilon}_L = \begin{Bmatrix} u_{0,x} \\ 0 \end{Bmatrix} - z\begin{Bmatrix} w_{b,xx} \\ 0 \end{Bmatrix} - f\begin{Bmatrix} w_{s,xx} \\ 0 \end{Bmatrix} + (1 - f')\begin{Bmatrix} 0 \\ w_{s,x} \end{Bmatrix}, \tag{5}$$

$$\boldsymbol{\varepsilon}_{NL} = \frac{1}{2}\left(\frac{\partial w_0}{\partial x}\right)^2 = \frac{1}{2}\begin{Bmatrix} (w_{b,x} + w_{s,x})^2 \\ 0 \end{Bmatrix}$$

here, $\boldsymbol{\varepsilon}_L$ and $\boldsymbol{\varepsilon}_{NL}$ represent the linear and nonlinear strain components, respectively.

The stress field $\boldsymbol{\sigma}$ is determined from the strain field $\boldsymbol{\varepsilon}$ using Hooke's law as follows:

$$\boldsymbol{\sigma} = \begin{Bmatrix} \sigma_x \\ \tau_{xz} \end{Bmatrix} = E(x,z)\begin{bmatrix} 1 & 0 \\ 0 & \dfrac{1}{2[1+\vartheta(x,z)]} \end{bmatrix}\boldsymbol{\varepsilon} = \mathbf{Q}\boldsymbol{\varepsilon} \tag{6}$$

The curvature components $\boldsymbol{\chi}$ (curvature tensor) are defined as follows:

$$\boldsymbol{\chi} = \begin{Bmatrix} \chi_{xy} \\ \chi_{yz} \end{Bmatrix}, \chi_{xy} = \frac{1}{2}\frac{\partial \theta_y}{\partial x}, \chi_{yz} = \frac{1}{2}\frac{\partial \theta_y}{\partial z} \tag{7}$$

in which

$$\theta_y = \frac{1}{2}\left(\frac{\partial u}{\partial z} - \frac{\partial w}{\partial x}\right) = -w_{b,x} - \frac{1}{2}(1 + f')w_{s,x} \tag{8}$$

Substituting the curvature expressions from Eq. (8) into Eq. (7), we obtain:

$$\boldsymbol{\chi} = -\frac{1}{2}\begin{Bmatrix} w_{b,xx} \\ 0 \end{Bmatrix} - \frac{1}{4}\begin{Bmatrix} (1+f')w_{s,xx} \\ f''w_{s,x} \end{Bmatrix} \tag{9}$$

The vector of the deviatoric components of the symmetric couple stress tensor $\mathbf{m}$ is defined by the following expression:

$$\mathbf{m} = \mathcal{M}\boldsymbol{\chi} \text{ with } \mathcal{M} = \frac{E(x,z)\ell^2(x,z)}{1+\vartheta(x,z)} \tag{10}$$

where $\ell(x,z)$ is a length-scale parameter.

Based on MCST, the variational form of the elastic strain energy potential in the beam is given by the following expression. [7]:

$$\delta U = \int_\Omega \boldsymbol{\sigma}^{\mathrm{T}}\delta\boldsymbol{\varepsilon}\, d\Omega + \int_\Omega 2\mathbf{m}^{\mathrm{T}}\delta\boldsymbol{\chi}\, d\Omega \tag{11}$$

The variational form of the elastic foundation potential energy can be expressed as

$$\delta U^f = \int_L \left[k_W w\delta w + k_G w_{,x}\delta w_{,x}\right]dx \tag{12}$$

The variational form of the work done by external forces acting on the McrB is given by

$$\delta W = \int_L q(x)\delta w dx \tag{13}$$

Based on the principle of minimum total potential energy, the equilibrium equations of the McrB are derived by

$$\delta U + \delta U^f - \delta W = 0 \tag{14}$$

4. Finite Element Procedure

Using a two-node beam element, where each node has five DOF, the displacement vector of the node $\mathbf{d}_e$ of the beam element has the following form:

$$\underset{10\times1}{\mathbf{d}_e} = [\mathbf{d}_m^{\mathrm{T}} \quad \mathbf{d}_b^{\mathrm{T}} \quad \mathbf{d}_s^{\mathrm{T}}]^{\mathrm{T}},$$

$$\underset{2\times1}{\mathbf{d}_m} = \{u_{01} \quad u_{02}\}^{\mathrm{T}}, \underset{4\times1}{\mathbf{d}_b} = \{w_{b1} \quad w_{b1,x} \quad w_{b2} \quad w_{b2,x}\}^{\mathrm{T}}, \quad \underset{4\times1}{\mathbf{d}_s} = \{w_{s1} \quad w_{s1,x} \quad w_{s2} \quad w_{s2,x}\}^{\mathrm{T}} \tag{15}$$

The displacement variables on the midplane of the beam element are approximated by

$$u_0 = \mathbf{N}\mathbf{d}_m, w_b = \mathbf{H}\mathbf{d}_b, w_s = \mathbf{H}\mathbf{d}_s \tag{16}$$

in which $\mathbf{N}$ and $\mathbf{H}$ are the Lagrange and Hermitian function matrices, respectively, defined by the following formula:

$$\mathbf{N} = [N_1 \quad N_2], \mathbf{H} = [H_1 \quad H_2 \quad H_3 \quad H_4],$$
$$N_1 = 1 - \eta, N_2 = \eta, H_1 = 1 - 3\eta^2 + 2\eta^3,$$
$$H_2 = \bar{x}(1 - 2\eta + \eta^2), H_3 = 3\eta^2 - 2\eta^3, H_4 = \bar{x}(-\eta + \eta^2), \eta = \frac{\bar{x}}{L_e}. \tag{17}$$

Here, $\bar{x}$ is the local coordinate following x direction, and L_e is the length of the beam element.

Substituting Eq. (16) into Eq. (3), the displacement field in an element is determined by

$$\mathbf{u} = \mathbf{N_u}\mathbf{d}_e,$$
$$\mathbf{N_u} = \begin{bmatrix} \mathbf{N}_u \\ \mathbf{N}_w \end{bmatrix} = \begin{bmatrix} \mathbf{N} & -z\mathbf{H}_{,x} & -f\mathbf{H}_{,x} \\ \mathbf{0} & \mathbf{H} & \mathbf{H} \end{bmatrix} \tag{18}$$

Substituting Eq. (16) into Eq. (5) and Eq. (9), the deformation field in the element is:

The linear strain vector $\boldsymbol{\varepsilon}_L$:

$$\boldsymbol{\varepsilon}_L = \mathbf{B}_{L1}\mathbf{d}_e, \underset{10\times 2}{\mathbf{B}_{L1}} = \begin{bmatrix} \mathbf{N}_{,x} & -z\mathbf{H}_{,xx} & -f\mathbf{H}_{,xx} \\ \mathbf{0} & \mathbf{0} & (1-f')\mathbf{H}_{,x} \end{bmatrix} \quad (19)$$

The nonlinear strain vector $\boldsymbol{\varepsilon}_{NL}$:

$$\boldsymbol{\varepsilon}_{NL} = \frac{1}{2}\begin{Bmatrix} w_{b,x}+w_{s,x} \\ 0 \end{Bmatrix}(w_{b,x}+w_{s,x}) = \frac{1}{2}\mathbf{B}_{NL}\mathbf{d}_e,$$
$$\mathbf{B}_{NL} = \begin{bmatrix} \mathbf{G}\mathbf{d}_e \\ 0 \end{bmatrix}\mathbf{G}; \mathbf{G} = [\mathbf{0} \quad \mathbf{H}_{,x} \quad \mathbf{H}_{,x}] \quad (20)$$

Curvature vector $\boldsymbol{\chi}$:

$$\boldsymbol{\chi} = \mathbf{B}_{L2}\mathbf{d}_e, \underset{10\times 2}{\mathbf{B}_{L2}} = -\frac{1}{4}\begin{bmatrix} \mathbf{0} & 2\mathbf{H}_{,xx} & (1+f')\mathbf{H}_{,xx} \\ \mathbf{0} & \mathbf{0} & f''\mathbf{H}_{,x} \end{bmatrix} \quad (21)$$

Substitute Eqs. (19) and (21) into Eq. (11) to get the variational potential energy of the elastic deformation of the beam element:

$$\delta U_e = \delta\mathbf{d}_e^{\mathrm{T}}\mathbf{K}_e\mathbf{d}_e,$$
$$\mathbf{K}_e = \int_{\Omega_e}(\mathbf{B}_{L1}+\mathbf{B}_{NL})^{\mathrm{T}}\mathbf{Q}\left(\mathbf{B}_{L1}+\frac{1}{2}\mathbf{B}_{NL}\right)d\Omega + \int_{\Omega_e}2\mathbf{B}_{L2}^{\mathrm{T}}\mathcal{M}\mathbf{B}_{L2}d\Omega \quad (22)$$

Substituting Eq. (16) into Eqs. (12) and (13), we get the variational expressions of the potential energy of the foundation element and the assignment of the external force as follows:

$$U_e^f = \delta\mathbf{d}_e^{\mathrm{T}}\mathbf{K}_e^f\mathbf{d}_e, \delta W_e = \delta\mathbf{d}_e^{\mathrm{T}}\mathbf{F}_e,$$
$$\mathbf{K}_e^f = \int_{L_e}\left[k_W\mathbf{N}_{w_0}^{\mathrm{T}}\mathbf{N}_{w_0} + k_G\mathbf{N}_{w_0,x}^{\mathrm{T}}\mathbf{N}_{w_0,x}\right]dx, \mathbf{F}_e = \int_{L_e}q(x)\mathbf{N}_{w_0}^{\mathrm{T}}dx \quad (23)$$

where $\mathbf{K}_e^f$ is the foundation stiffness and $\mathbf{F}_e$ is the nodal load of an element.

Substituting Eqs. (22) and (23) into Eq. (14), the system of nonlinear static equilibrium equations of the beam element is:

$$(\mathbf{K}_e + \mathbf{K}_e^f)\mathbf{d}_e - \mathbf{F}_e = \mathbf{0} \quad (24)$$

Eq. (24) is rewritten as

$$\mathbf{R}(\mathbf{d}_e) = \mathbf{F}_e^{in}(\mathbf{d}_e) - \mathbf{F}_e^{out} = \mathbf{0},$$
$$\mathbf{F}_e^{in}(\mathbf{d}_e) = (\mathbf{K}_e + \mathbf{K}_e^f)\mathbf{d}_e, \mathbf{F}_e^{out} = \mathbf{F}_e \quad (25)$$

where, $\mathbf{R}(\mathbf{d}_e)$ is called the residual force vector, $\mathbf{F}_e^{in}(\mathbf{d}_e)$ and $\mathbf{F}_e^{out}$ are the internal force vector and external force vector of the element, respectively

The nonlinear static equilibrium equation system of the McrB is obtained after assembling the elements, as follows

$$\mathbf{R}(\mathbf{D},\lambda) = \mathbf{F}^{in}(\mathbf{D}) - \lambda\mathbf{F}^{out} = \mathbf{0} \quad (26)$$

where, $\mathbf{R}(\mathbf{D},\lambda)$ is the overall residual force vector, $\mathbf{D}$ is the overall nodal displacement vector, $\mathbf{F}^{in}$ and $\mathbf{F}^{out}$ are the overall internal and external force vectors collected from $\mathbf{F}_e^{in}$ and $\mathbf{F}_e^{out}$ respectively, and $\lambda \in [0;1]$ is the load parameter.

The nonlinear Eq. (26) is solved based on the use of the Newton-Raphson iteration algorithm for each load level. [43], the load levels are divided according to the parameter λ_n ($n = 1;2;3\ldots$). Accordingly, the node displacement vector in the $i+1$ iteration step is determined as follows:

$$\mathbf{D}_n^{i+1} = \mathbf{D}_n^i + \Delta\mathbf{D}_n^{i+1} \quad (27)$$

where $\Delta\mathbf{D}_n^{i+1}$ is the displacement increment, defined by the expression:

$$\Delta\mathbf{D}_n^{i+1} = -[\mathbf{K}_T(\mathbf{D}_n^i)]^{-1}\mathbf{R}(\mathbf{D}_n^i,\lambda_n) \quad (28)$$

where $\mathbf{K}_T$ is the overall tangent stiffness matrix, which is collected from the element tangent stiffness matrix $\mathbf{K}_{eT}$. The $\mathbf{K}_{eT}$ matrix has the following expression:

$$\mathbf{K}_{eT} = \frac{\partial\mathbf{R}(\mathbf{d}_e)}{\partial\mathbf{d}_e} = \frac{\partial\mathbf{F}_e^{in}(\mathbf{d}_e)}{\partial\mathbf{d}_e} = \mathbf{K}_e^L + \mathbf{K}_e^{NL} + \mathbf{K}_e^f + \mathbf{K}_e^\sigma,$$
$$\mathbf{K}_e^L = \int_{\Omega_e}\mathbf{B}_{L_1}^{\mathrm{T}}\mathbf{Q}\mathbf{B}_{L_1}d\Omega + \int_{\Omega_e}2\mathbf{B}_{L2}^{\mathrm{T}}\mathcal{M}\mathbf{B}_{L2}d\Omega, \mathbf{K}_e^\sigma = \int_{\Omega_e}\mathbf{G}^{\mathrm{T}}\sigma_x\mathbf{G}d\Omega, \quad (29)$$
$$\mathbf{K}_e^{NL} = \int_{\Omega_e}(\mathbf{B}_{L_1}^{\mathrm{T}}\mathbf{Q}\mathbf{B}_{NL} + \mathbf{B}_{NL}^{\mathrm{T}}\mathbf{Q}\mathbf{B}_{L_1} + \mathbf{B}_{NL}^{\mathrm{T}}\mathbf{Q}\mathbf{B}_{NL})d\Omega$$

and the residual force vector $\mathbf{R}(\mathbf{D}_n^i,\lambda_n)$ is determined by Eq. (26).

Note that the element matrices and element node load vectors in formulas (23) and (29) are calculated by Gauss quadrature numerical integration method.

To solve Eq. (28), it is necessary to have the initial value of the displacement in each load level, specifically in this paper, $\mathbf{D}_1^0 = \mathbf{0}$ and $\mathbf{D}_n^0 = \mathbf{D}_{n-1}$. The convergence condition is checked after each loop according to the following expression:

$$\|\mathbf{R}(\mathbf{D}_n^i,\lambda_n)\| \le \psi\|\lambda_n\mathbf{F}^{out}\| \quad (30)$$

where ψ is the error, chosen to be 10^{-4}.

The Eq. (28) is solved with the given BCs. In this paper, BCs are shown in Table 1.

Table 1. Boundary conditions of McrBs

BCs	At $x = 0$	At $x = L$
CF	$u_0 = w_b = w_s = w_{b,x} = w_{s,x} = 0$	freedom
SS	$u_0 = w_b = w_s = 0$	$u_0 = w_b = w_s = 0$
CS	$u_0 = w_b = w_s = w_{b,x} = w_{s,x} = 0$	$u_0 = w_b = w_s = 0$
CC	$u_0 = w_b = w_s = w_{b,x} = w_{s,x} = 0$	$u_0 = w_b = w_s = w_{b,x} = w_{s,x} = 0$

5. Numerical Results and Discussion

In the following sections, except for the comparative verification results, material components for 2DFG-McrBs are composed of two component material phases: the ceramic phase (SiC) and the metal phase (Al), with the properties given in Table 2. The results for the case $\bar{h}=\infty$ are calculated for normal beams (macrobeams).

Table 2. Material properties of the component materials [44]

Componentes	Symbol	E (GPa)	ϑ	ℓ(μm)
SiC	c	427	0.17	22.5
Al	m	70	0.3	15

Some dimensionless quantities used in the paper are defined by the following expressions:

$$w^*=\frac{100E_mI}{q_0L^4}w\left(\frac{L}{2}\right),$$
$$\sigma_x^*(z)=\frac{bh}{q_0L}\sigma\left(\frac{L}{2},z\right),$$
$$\sigma_{xz}^*(z)=\frac{bh}{q_0L}\tau(0,z), \tag{31}$$
$$h^*=\frac{h}{\ell_c},\bar{Q}=\frac{q_0L^4}{E_mbh^4},$$
$$K_W=\frac{k_WL^4}{E_mI},K_G=\frac{k_GL^2}{E_mI},I=\frac{bh^3}{12}$$

5.1. Verification

Firstly, Table 3 lists the comparison result of linear static displacement parameter $\widehat{W}=\frac{100E_mbh^3}{q_0L^4}w\left(\frac{L}{2}\right)$ and linear static stress parameters for SS 2DFG macrobeams under uniformly distributed force (q_0) between the present method and those of Karamali [45] using an exact solution based on Quasi-3D. In which the beam is made of ceramic (Al_2O_3) and metal (Al) with characteristics $E_c=380GPa,\vartheta_c=0.3$ và $E_m=70GPa,\vartheta_m=0.3$. The result is calculated with $n_z=0.5$. It can be seen that the results converge at a uniform mesh size of $nE=18$ and are close to the results of Karamali [45] with an error of approximately 1%.

Secondly, Table 4 shows the result of comparing the nonlinear displacement parameter $w^{**}=\frac{100Ebh^3}{12L^4}w\left(\frac{L}{2}\right)$ of SS homogeneous McrBs under uniformly distributed force (q_0) with geometric dimensions: $L=250\mu m, h=3\mu m, b=50\mu m$, and material properties as $E=169MPa$, $\vartheta=0{,}06$. Observing that the obtained results also converge at a uniform mesh size of $nE=18$ and are in good agreement with the results of Dang et al. [46] with an error of nearly 1%. From the above two examples, the accuracy and reliability of the proposed algorithm and calculation program can be confirmed. To ensure the smoothness of the deformation field, we use a uniform mesh size of $nE=20$ for further studies.

5.2. Nonlinear Static Response

First, Figure 4 illustrates the influence of different load types on the static response of SS 2DFG-McrBs, given the following input parameters: $\ell_c=22.5\mu m$, $\ell_m=15\mu m$, $h=4\ell_c$, $b=h$, $L=20h$, $K_W=50$, and $K_G=10$. Using the same input parameters, Figure 5 presents the static response of CC 2DFG-McrBs. The results indicate that the 2DFG-McrB under UL exhibits the largest displacement response, followed by beams under SL, LL, and PL. Moreover, for 2DFG-McrBs under LL and PL, the displacement curve is asymmetric, with the maximum displacement shifting toward the region experiencing the higher distributed force. Besides, the transverse shear stress σ_{xz}^* distribution follows a parabolic profile, reaching zero at the top and bottom surfaces for SS 2DFG-McrBs. For CC 2DFG-McrB, the shear stress is theoretically predicted to be zero across the entire edge thickness at the clamped boundary (Fig. 5d).

Second, Tables 5, 6, and 7 illustrate the effects of the power-law indexes in the x and z directions (n_x, n_z) on the displacement, normal stress, and shear stress of SS 2DFG-McrBs for different values of the parameter h^*. It can be observed that increasing n_x and/or n_z results in a higher beam displacement, as these parameters reduce the ceramic volume fraction, thereby decreasing the beam's stiffness. Furthermore, an increase in h^* leads to a larger displacement of the 2DFG-McrB. This occurs because a higher h^* corresponds to a decrease in the length scale, which in turn reduces the total elastic energy and, consequently, the beam's stiffness. As h^* approaches infinity, the beam displacement increases significantly, corresponding to the macroscopic case mentioned earlier.

Third, Figure 6 illustrates the influence of foundation stiffness (K_W, K_G) on the displacement of SS 2DFG-McrBs under different loading conditions and various values of the parameter h^* (which is related to the length-scale parameter). It can be observed that an increase in foundation stiffness reduces the beam's displacement, as expected. This is because the EF contributes to the total energy of the system, making the beam "stiffer." Furthermore, an increase in h^* (corresponding to a decrease in the length scale) leads to greater beam displacement, with the maximum displacement occurring in the macroscopic beam case ($h^*\to\infty$). Additionally, the shear layer provides more effective support than the spring layer, as anticipated.

Next, Figure 7 provides a more detailed illustration of how the length-scale parameter on the static response of CC 2DFG-McrBs under PL, through the dimensionless parameter h^*. From the results, it is evident that incorporating the length-scale parameter, particularly at higher values of h^*, significantly enhances the overall stiffness of the McrBs. Physically, this can be attributed to the size-dependent effects captured by the SGET, which become increasingly prominent at micro- and nano-scales, where classical theories tend to underestimate structural rigidity. As the effective stiffness increases, the beam's ability to resist deformation under external loading improves, thereby reducing the observed deflections. Furthermore, the displacement evolution across different load steps exhibits smooth and continuous curve profiles, aligning with theoretical expectations for such micro-scale structures. This consistency reaffirms the validity of the applied model in capturing the essential mechanical behaviors of FG-McrBs.

Furthermore, Figures. 8 and 9 respectively depict the effects of the material gradation indices n_x and/or n_z on the static response of 2DFG-McrBs under CC and CS boundaries. As anticipated, increasing the values of n_x and/or n_z results in larger beam displacements. This phenomenon is fundamentally linked to the material distribution across the beam's length and thickness: higher values of n_x and/or n_z correspond to a reduced volume fraction of the stiffer ceramic phase, leading to a more metal-rich composition. Since metals generally possess lower elastic moduli compared to ceramics, the overall stiffness of the beam diminishes as the gradation indices increase. Consequently, the beam exhibits a more compliant (flexible) response under applied loading. Another physically meaningful observation lies in the load–load-displacement behavior. Specifically, for cases involving the CC boundary, the displacement-load step curves tend to maintain a nearly linear relationship, resembling straight lines. This characteristic reflects the dominance of linear elastic bending behavior in the regime of small deformations, where geometric nonlinearity remains negligible.

Finally, Figure 10 presents a comprehensive comparison of how different BCs affect the static response of 2DFG-McrBs subjected to UL. As theoretically anticipated, the maximum displacement of the beam exhibits a clear increasing trend following the order of boundary constraint severity: CC, CS, SS, CF boundaries. This behavior is fundamentally governed by the degree of kinematic restrictions imposed at the beam ends. Specifically, the CC boundary provides the most rigid constraint by restraining both translations and rotations, thereby minimizing deflection. Conversely, the CF boundary, commonly referred to as a cantilever beam, allows for maximal deformation due to the absence of support at the free end. An important physical insight is revealed through the symmetry (or asymmetry) of the displacement profiles. For beams with symmetric BCs, such as CC and SS boundaries, the displacement response curves maintain geometric symmetry about the beam's midspan. This is a direct consequence of the uniform distribution of constraints and loading, which enforces a balanced deformation pattern. On the other hand, in configurations where BCs are asymmetric (e.g., CS and CF boundaries), the displacement curves exhibit noticeable asymmetry, with the deformation profile skewing towards the less restrictive (weaker) boundary. This deviation reflects the beam's natural tendency to bend more freely where constraints are minimal, highlighting the critical role of BCs in dictating the mode shapes.

Table 3. Comparison results of the static response of SS 2DFG macrobeams with different mesh sizes

L/h	Parameters	Methods	Power-law index				
			$n_x = 0$	$n_x = 0.1$	$n_x = 0.5$	$n_x = 1$	$n_x = 2$
10	w^*	Karamali [45]	4.5015	4.5957	4.9843	5.4912	6.5521
		Present					
		$nE = 12$	4.5304	4.6244	5.0125	5.5224	6.6008
		$nE = 14$	4.5308	4.6248	5.0130	5.5229	6.6013
		$nE = 16$	4.5311	4.6251	5.0133	5.5232	6.6016
		$nE = 18$	4.5315	4.6255	5.0137	5.5235	6.6018
		$nE = 20$	4.5315	4.6255	5.0137	5.5235	6.6019
		Error (%)	0.6664	0.6484	0.5899	0.5882	0.7601
	$\sigma_x^*(h/2)$	Karamali [45]	9.8766	9.5863	9.7674	9.6417	9.3574
		Present					
		$nE = 12$	9.9270	9.9046	9.8133	9.6963	9.4573
		$nE = 14$	9.9116	9.8893	9.7987	9.6824	9.4439
		$nE = 16$	9.9016	9.8795	9.7894	9.6735	9.4354
		$nE = 18$	9.8898	9.8679	9.7785	9.6633	9.4257
		$nE = 20$	9.8898	9.8679	9.7785	9.6634	9.4258
		Error (%)	0.1336	2.9375	0.1136	0.2251	0.7310
	$\sigma_{xz}^*(0)$	Karamali [45]	0.7532	0.7598	0.7852	0.8143	0.8617
		Present					
		$nE = 12$	0.7655	0.7721	0.7975	0.8265	0.8733
		$nE = 14$	0.7648	0.7714	0.7969	0.8259	0.8729
		$nE = 16$	0.7642	0.7708	0.7963	0.8254	0.8725

		$nE = 18$	0.7632	0.7697	0.7952	0.8244	0.8716
		$nE = 20$	0.7632	0.7698	0.7953	0.8245	0.8717
		Error (%)	1.3277	1.3161	1.2863	1.2526	1.1605
20	w^*	Karamali [45]	4.4347	4.5274	4.9092	5.4076	6.4513
		Present					
		$nE = 12$	4.4575	4.5498	4.9309	5.4319	6.4931
		$nE = 14$	4.4580	4.5502	4.9314	5.4324	6.4936
		$nE = 16$	4.4583	4.5505	4.9317	5.4327	6.4939
		$nE = 18$	4.4586	4.5508	4.9320	5.4329	6.4941
		$nE = 20$	4.4586	4.5509	4.9321	5.4330	6.4942
		Error (%)	0.5389	0.5191	0.4665	0.4697	0.6650
	$\sigma_x^*(h/2)$	Karamali [45]	19.7048	19.6642	19.4863	19.2343	18.6648
		Present					
		$nE = 12$	19.8006	19.7559	19.5738	19.3410	18.8663
		$nE = 14$	19.7697	19.7253	19.5446	19.3131	18.8394
		$nE = 16$	19.7497	19.7055	19.5259	19.2953	18.8224
		$nE = 18$	19.7260	19.6822	19.5040	19.2749	18.8029
		$nE = 20$	19.7261	19.6823	19.5041	19.2750	18.8031
		Error (%)	0.1081	0.0920	0.0913	0.2116	0.7410
	$\sigma_{xz}^*(0)$	Karamali [45]	0.7599	0.7667	0.7933	0.8240	0.8750
		Present					
		$nE = 12$	0.7688	0.7754	0.8006	0.8293	0.8755
		$nE = 14$	0.7687	0.7752	0.8004	0.8292	0.8754
		$nE = 16$	0.7685	0.7750	0.8002	0.8290	0.8753
		$nE = 18$	0.7680	0.7745	0.7998	0.8285	0.8749
		$nE = 20$	0.7681	0.7746	0.7999	0.8286	0.8750
		Error (%)	1.0791	1.0304	0.8320	0.5583	0.0000

Table 4. Comparison results of the nonlinear displacement of SS McrBs

BCs	q_0	Methods	ℓ/h				
			0.1	0.2	0.4	0.6	0.9
CC	5	Dang et al. [46]	0.9545	0.8764	0.6374	0.4204	0.2324
		Present					
		$nE = 12$	0.9475	0.8711	0.6358	0.4203	0.2325
		$nE = 14$	0.9490	0.8722	0.6362	0.4204	0.2325
		$nE = 16$	0.9500	0.8730	0.6365	0.4204	0.2325
		$nE = 18$	0.9511	0.8738	0.6367	0.4205	0.2324
		$nE = 20$	0.9512	0.8739	0.6368	0.4205	0.2325
		Error (%)	0.3457	0.2853	0.0941	0.0238	0.0430
	10	Dang et al. [46]	1.4633	1.3877	1.1185	0.8003	0.4604
		Present					
		$nE = 12$	1.4483	1.3744	1.1114	0.7982	0.4604
		$nE = 14$	1.4516	1.3773	1.1129	0.7987	0.4604
		$nE = 16$	1.4538	1.3792	1.1139	0.7991	0.4605
		$nE = 18$	1.4562	1.3813	1.1150	0.7994	0.4604
		$nE = 20$	1.4563	1.3814	1.1151	0.7995	0.4605
		Error (%)	0.4784	0.4540	0.3040	0.1000	0.0217
SS	5	Dang et al. [46]	1.5142	1.4917	1.4000	1.2492	0.9517
		Present					
		$nE = 12$	1.4970	1.4749	1.3854	1.2383	0.9467
		$nE = 14$	1.4980	1.4759	1.3864	1.2391	0.9471
		$nE = 16$	1.4986	1.4766	1.3870	1.2396	0.9474
		$nE = 18$	1.4993	1.4773	1.3878	1.2402	0.9476
		$nE = 20$	1.4994	1.4774	1.3878	1.2402	0.9477
		Error (%)	0.9774	0.9586	0.8714	0.7205	0.4203
	10	Dang et al. [46]	1.9704	1.9538	1.8837	1.7624	1.4965
		Present					
		$nE = 12$	1.9481	1.9315	1.8626	1.7442	1.4845
		$nE = 14$	1.9492	1.9327	1.8638	1.7454	1.4854
		$nE = 16$	1.9499	1.9334	1.8646	1.7462	1.4860
		$nE = 18$	1.9507	1.9342	1.8655	1.7472	1.4866
		$nE = 20$	1.9508	1.9343	1.8656	1.7472	1.4866
		Error (%)	0.9947	0.9981	0.9609	0.8625	0.6615

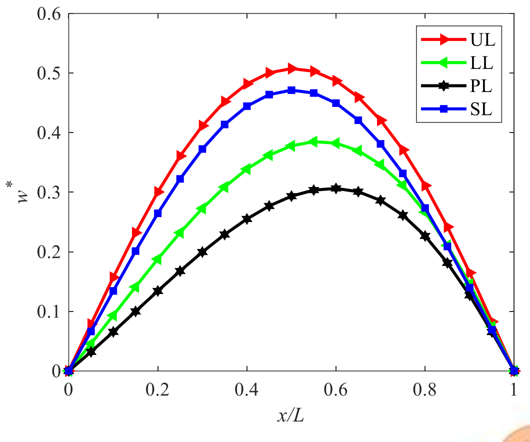

a) The displacement field

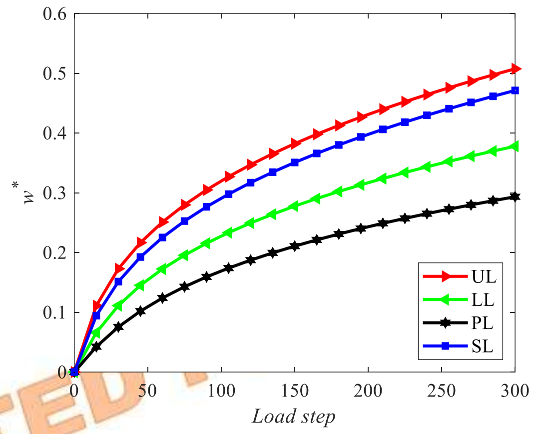

b) Displacement by load step

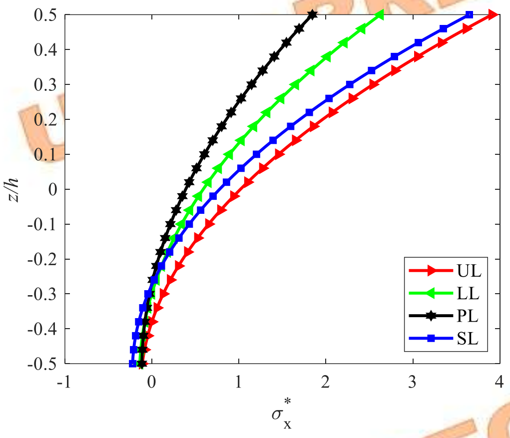

c) Normal stress $\sigma_x^*(z)$

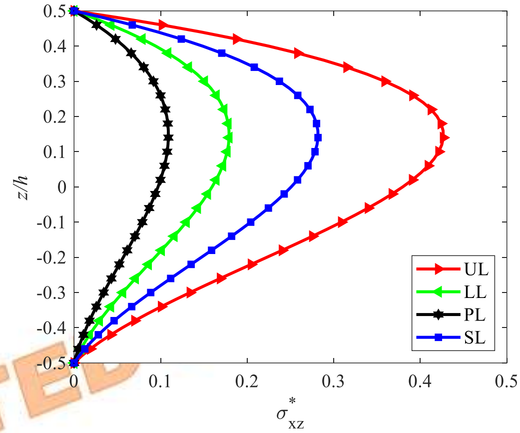

d) Shear stress $\sigma_{xz}^*(z)$

Fig. 4. Effect of load types on the nonlinear static response of SS 2DFG-McrBs

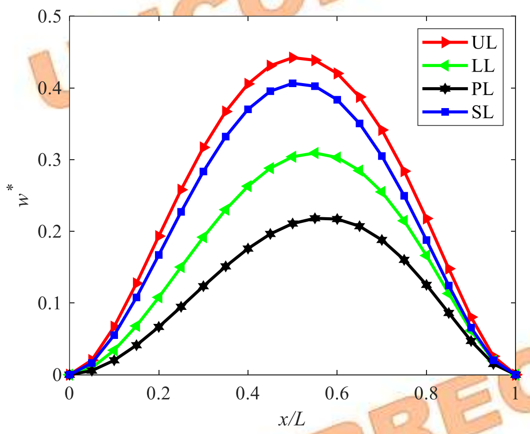

a) The displacement field

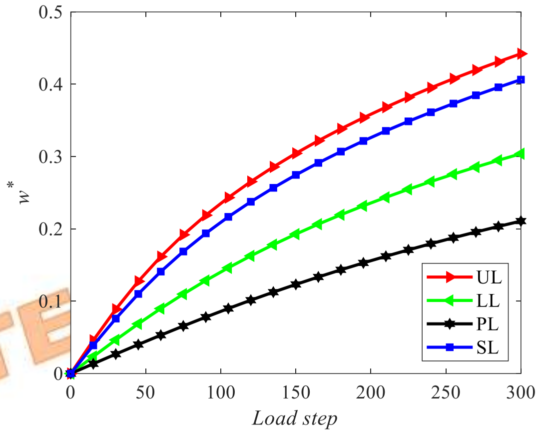

b) Displacement by load step

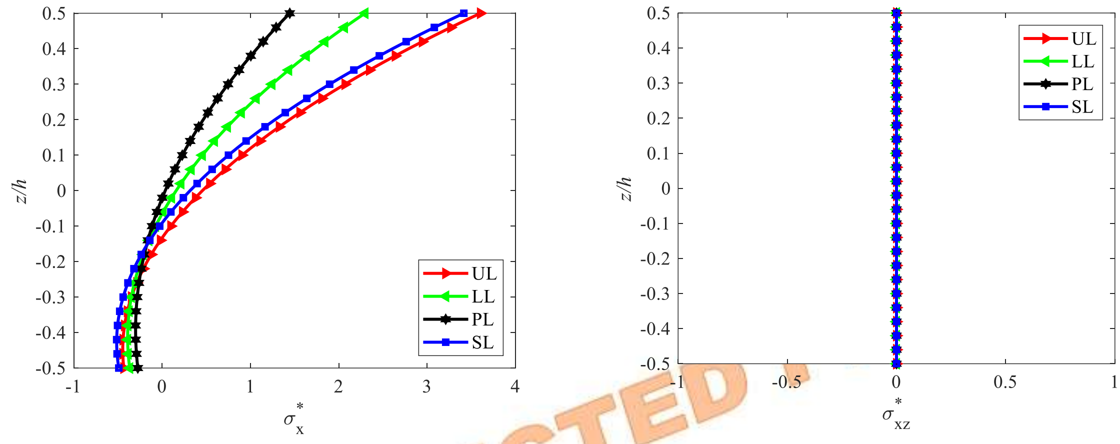

c) Normal stress $\sigma_x^*(z)$ d) Shear stress $\sigma_{xz}^*(z)$

Fig. 5. Effect of load types on the nonlinear static response of CC 2DFG-McrBs

Table 5. Nonlinear displacement w^* of SS 2DFG-McrB under UL
(Input parameters: $\bar{Q} = 300$; $L = 30h$; $K_W = 75$; $K_G = 15$)

h^*	n_z	Power-law index					
		$n_x = 0$	0.5	1	2	5	10
1	0	0.2904	0.3247	0.3570	0.4160	0.5495	0.6517
	0.5	0.3544	0.3837	0.4116	0.4633	0.5792	0.6652
	1	0.3920	0.4194	0.4456	0.4939	0.5988	0.6747
	2	0.4427	0.4682	0.4922	0.5355	0.6253	0.6879
	5	0.5271	0.5484	0.5679	0.6015	0.6659	0.7078
	10	0.5936	0.6102	0.6249	0.6494	0.6935	0.7207
2	0	0.3816	0.4053	0.4286	0.4742	0.5869	0.6743
	0.5	0.4189	0.4415	0.464	0.5074	0.6091	0.6854
	1	0.4467	0.4689	0.4907	0.5322	0.6255	0.6942
	2	0.4887	0.51	0.5305	0.5684	0.6493	0.7071
	5	0.5629	0.5812	0.5982	0.6282	0.6873	0.7268
	10	0.6228	0.6373	0.6504	0.6726	0.7135	0.7393
4	0	0.4052	0.4256	0.4465	0.4885	0.5956	0.6788
	0.5	0.4353	0.456	0.4769	0.5181	0.6157	0.6894
	1	0.4609	0.4815	0.502	0.5416	0.6315	0.6982
	2	0.501	0.5209	0.5403	0.5765	0.6547	0.7113
	5	0.5723	0.5896	0.6058	0.6347	0.6922	0.731
	10	0.6299	0.6438	0.6565	0.678	0.7179	0.7434
8	0	0.4109	0.4305	0.4507	0.4919	0.5975	0.6797
	0.5	0.4393	0.4595	0.4801	0.5206	0.6172	0.6902
	1	0.4645	0.4847	0.5049	0.5438	0.6328	0.6991
	2	0.5042	0.5237	0.5428	0.5785	0.656	0.7123
	5	0.5747	0.5917	0.6077	0.6363	0.6934	0.7321
	10	0.6317	0.6455	0.658	0.6793	0.719	0.7444
∞	0	0.4127	0.4321	0.4521	0.493	0.5982	0.68
	0.5	0.4406	0.4607	0.4811	0.5215	0.6177	0.6905
	1	0.4657	0.4857	0.5058	0.5446	0.6333	0.6994
	2	0.5053	0.5247	0.5436	0.5792	0.6565	0.7127
	5	0.5755	0.5924	0.6084	0.6368	0.6938	0.7324
	10	0.6323	0.646	0.6585	0.6797	0.7194	0.7447

Table 6. Normal stress $\sigma_x^*(h/2)$ of SS 2DFG-McrB under UL
(Input parameters: $\bar{Q} = 300$; $L = 30h$; $K_W = 75$; $K_G = 15$)

h^*	n_z	Power-law index					
		$n_x = 0$	0.5	1	2	5	10
1	0	3.6627	3.7622	3.7975	3.7398	3.2622	2.68
	0.5	4.6257	4.577	4.4898	4.2526	3.4968	2.7282
	1	5.2187	5.0969	4.9478	4.6125	3.6704	2.7611
	2	6.0923	5.8737	5.6394	5.16	3.9204	2.8012
	5	7.8139	7.3903	6.9706	6.1726	4.3105	2.8466

	10	9.425	8.762	8.1324	6.9923	4.5624	2.8653
2	0	5.2085	5.0154	4.8166	4.4308	3.5212	2.7602
	0.5	5.7821	5.5189	5.263	4.7868	3.7048	2.8091
	1	6.2282	5.9216	5.6271	5.0841	3.8592	2.8445
	2	6.9657	6.5895	6.2308	5.5737	4.0953	2.888
	5	8.5404	7.9894	7.4695	6.5285	4.4761	2.9356
	10	10.0619	9.2911	8.5768	7.3161	4.7229	2.9535
4	0	5.5961	5.3108	5.0448	4.5708	3.5540	2.7619
	0.5	6.0641	5.7383	5.4348	4.8931	3.7308	2.8162
	1	6.4737	6.1134	5.7774	5.1770	3.8839	2.8546
	2	7.1740	6.7533	6.3601	5.6549	4.1210	2.9012
	5	8.7068	8.1226	7.5766	6.5993	4.5048	2.9512
	10	10.2041	9.4064	8.6709	7.3809	4.7525	2.9694
8	0	5.6795	5.3732	5.0917	4.5972	3.557	2.7604
	0.5	6.1288	5.7872	5.4714	4.9131	3.7328	2.8165
	1	6.5314	6.1568	5.8097	5.1943	3.8861	2.856
	2	7.2232	6.7906	6.3881	5.6703	4.1244	2.9035
	5	8.7466	8.1535	7.6005	6.6138	4.5101	2.9544
	10	10.2386	9.4336	8.6924	7.395	4.7586	2.9728
∞	0	5.7050	5.3922	5.1058	4.6048	3.5574	2.7597
	0.5	6.1498	5.8026	5.4826	4.9186	3.7328	2.8165
	1	6.5505	6.1707	5.8196	5.1990	3.8862	2.8563
	2	7.2397	6.8026	6.3967	5.6745	4.1250	2.9042
	5	8.7602	8.1637	7.6080	6.6180	4.5115	2.9553
	10	10.2506	9.4426	8.6994	7.3993	4.7604	2.9738

Table 7. Shear stress $\sigma_{xz}^{*}(0)$ of SS 2DFG-McrB under UL
(Input parameters: $\bar{Q} = 300$; $L = 30h$; $K_W = 75$; $K_G = 15$)

h^*	n_z	Power-law index					
		$n_x = 0$	0.5	1	2	5	10
1	0	0.0804	0.0808	0.0801	0.0764	0.0619	0.0456
	0.5	0.1926	0.1970	0.1991	0.1984	0.1847	0.1703
	1	0.2422	0.2456	0.2468	0.2448	0.2312	0.2200
	2	0.2369	0.2381	0.2379	0.2348	0.2240	0.2169
	5	0.1579	0.1578	0.1572	0.1552	0.1499	0.1461
	10	0.1320	0.1319	0.1315	0.1301	0.1264	0.1229
2	0	0.1307	0.1305	0.1293	0.1251	0.1055	0.0766
	0.5	0.3361	0.3345	0.3313	0.3216	0.29	0.259
	1	0.4219	0.4181	0.4129	0.4002	0.3663	0.3388
	2	0.4157	0.4109	0.4054	0.3935	0.3659	0.3457
	5	0.2719	0.2694	0.2665	0.2605	0.247	0.2356
	10	0.2158	0.2143	0.2125	0.2087	0.1996	0.1899
4	0	0.1636	0.164	0.1633	0.1588	0.1332	0.0893
	0.5	0.3396	0.3376	0.3344	0.3252	0.2924	0.2519
	1	0.4243	0.4203	0.4154	0.4037	0.3699	0.335
	2	0.4358	0.4309	0.4254	0.4138	0.3852	0.3587
	5	0.3032	0.3002	0.297	0.2903	0.2745	0.2577
	10	0.2391	0.2369	0.2346	0.2299	0.218	0.2032
8	0	0.1751	0.1751	0.1740	0.1682	0.1368	0.0828
	0.5	0.2999	0.2995	0.2978	0.2915	0.2624	0.2187
	1	0.3756	0.3739	0.3712	0.3635	0.3356	0.2992
	2	0.4010	0.3980	0.3943	0.3859	0.3616	0.3340
	5	0.2955	0.2930	0.2902	0.2843	0.2690	0.2503
	10	0.2345	0.2322	0.2299	0.2252	0.2126	0.1957
∞	0	0.1784	0.1780	0.1764	0.1697	0.1345	0.0754
	0.5	0.2733	0.2739	0.2732	0.2687	0.2420	0.1973
	1	0.3441	0.3438	0.3425	0.3374	0.3132	0.2767
	2	0.3768	0.3750	0.3726	0.3661	0.3447	0.3170
	5	0.2872	0.2851	0.2826	0.2773	0.2626	0.2432
	10	0.2290	0.2267	0.2244	0.2199	0.2072	0.1895

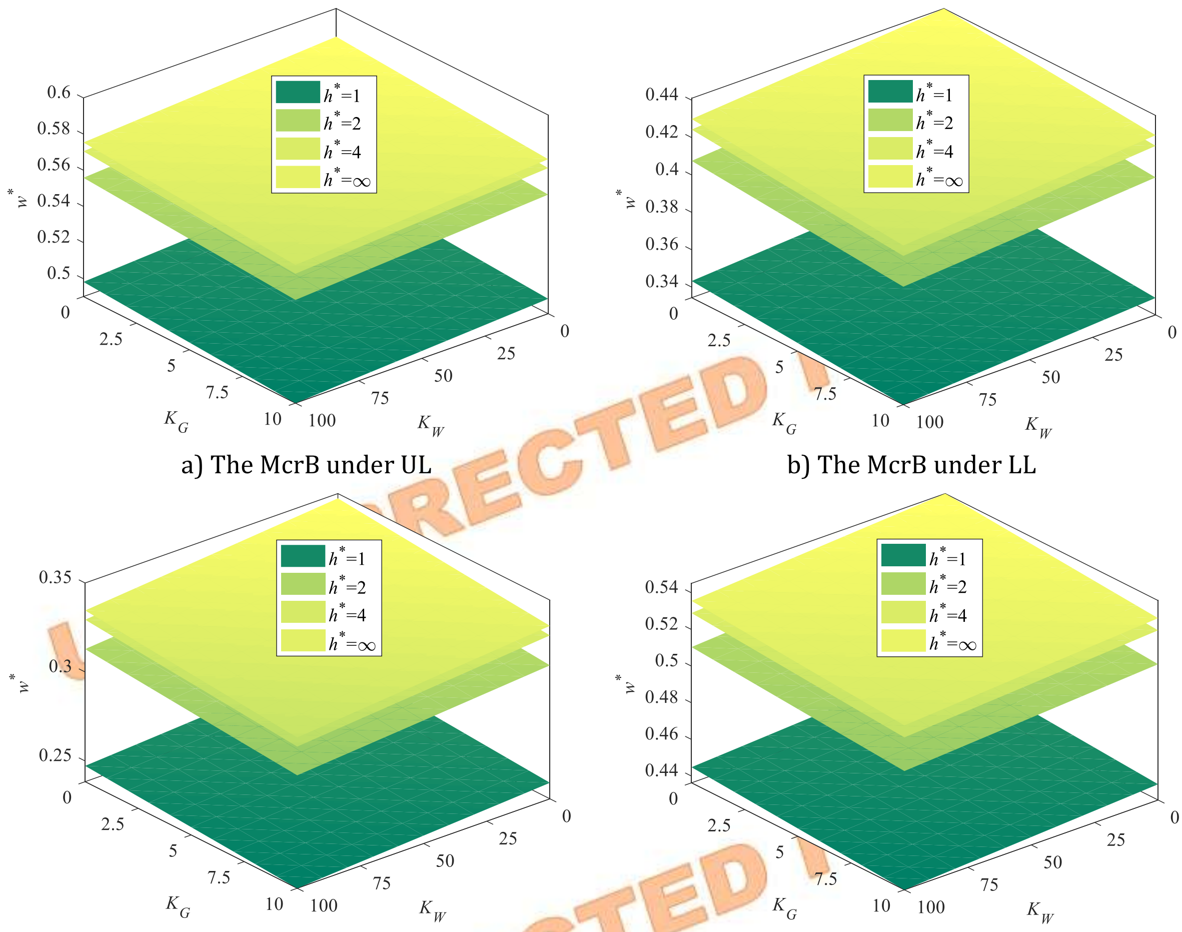

a) The McrB under UL
b) The McrB under LL
c) The McrB under PL
d) The McrB under SL

Fig. 6. Effect of the foundation stiffness (K_W, K_G) on the nonlinear displacement of SS 2DFG-McrBs under LL (Input parameter: $\bar{Q} = 250$; $L = 30h$; $n_x = n_z = 1$)

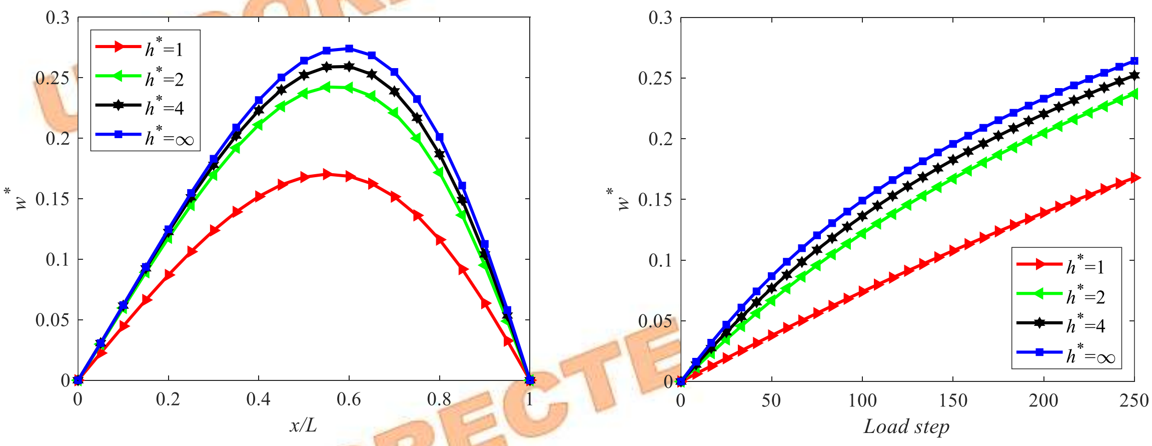

a) The displacement field
b) Displacement by load step

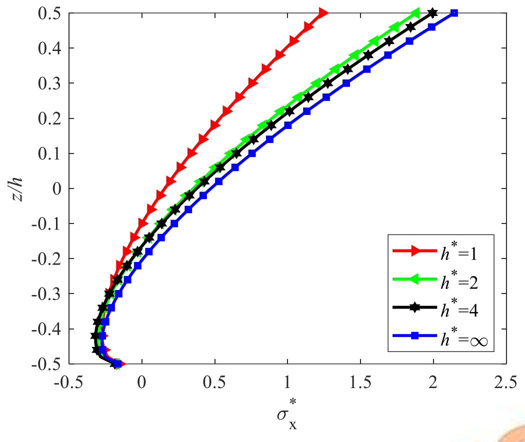

c) Normal stress $\sigma_x^*(z)$

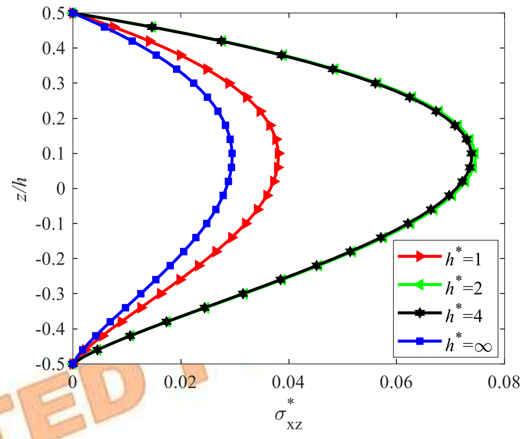

d) Shear stress $\sigma_{xz}^*(z)$

Fig. 7. Effect of the parameter h^* on the nonlinear static response of SS 2DFG-McrBs under PL (Input parameter: $\bar{Q} = 250$; $L = 25h$; $n_x = n_z = 0.5$; $K_W = K_G = 50$)

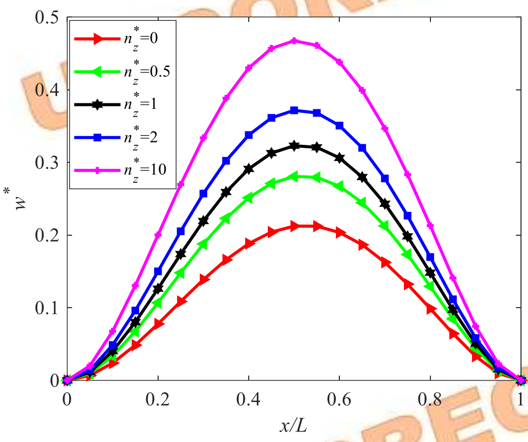

a) The displacement field

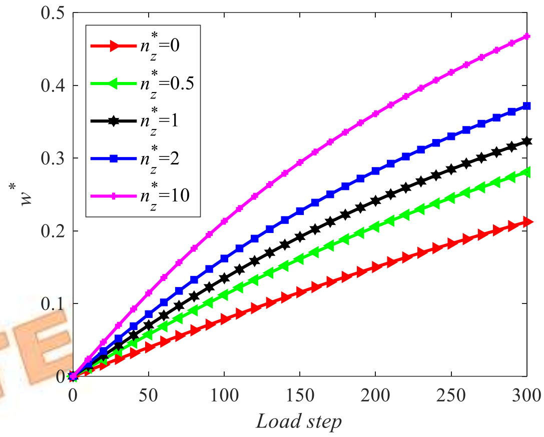

b) Displacement by load step

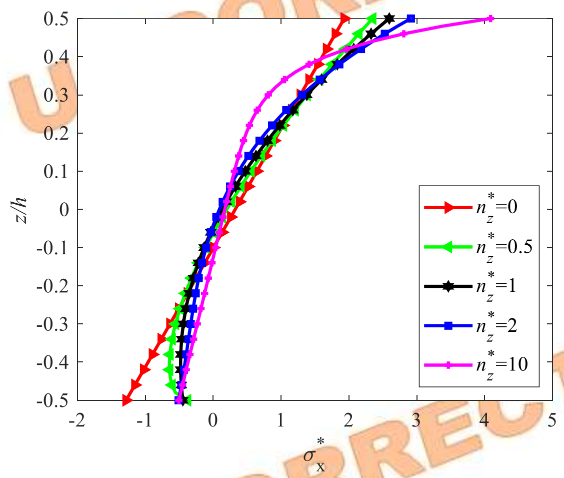

c) Normal stress $\sigma_x^*(z)$

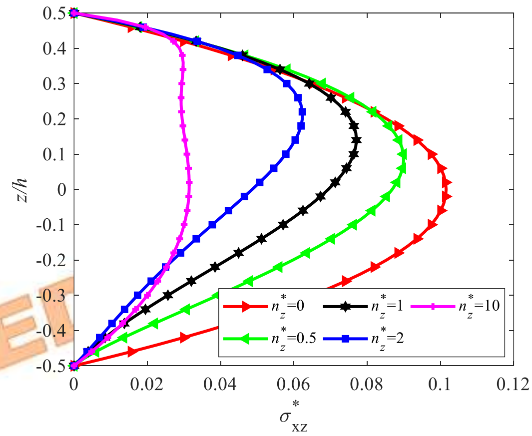

d) Shear stress $\sigma_{xz}^*(z)$ at $x = L/3$

Fig. 8. Effect of the parameter n_z on the nonlinear static response of CC 2DFG-McrBs under SL (Input parameter: $\bar{Q} = 300$; $L = 20h$; $n_x = 1$; $K_W = 75$; $K_G = 50$; $h^* = 2$)

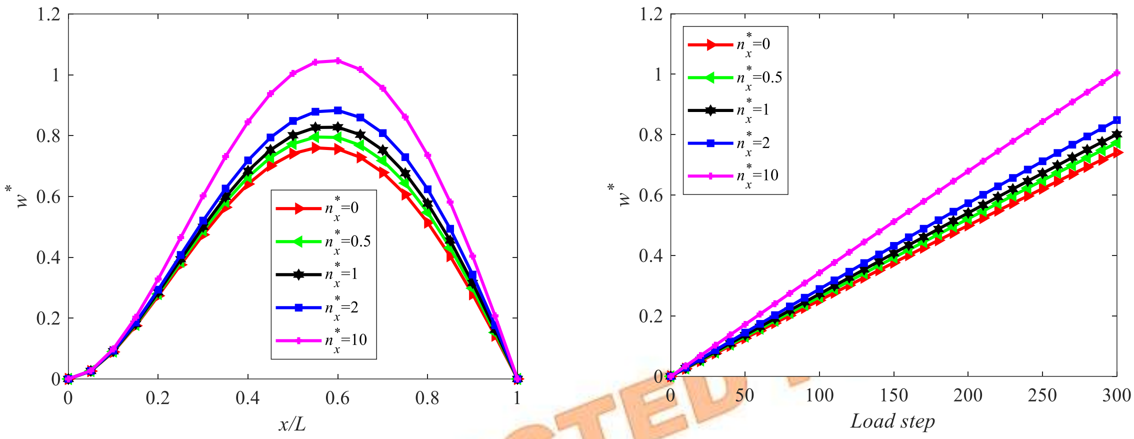

a) The displacement field b) Displacement by load step

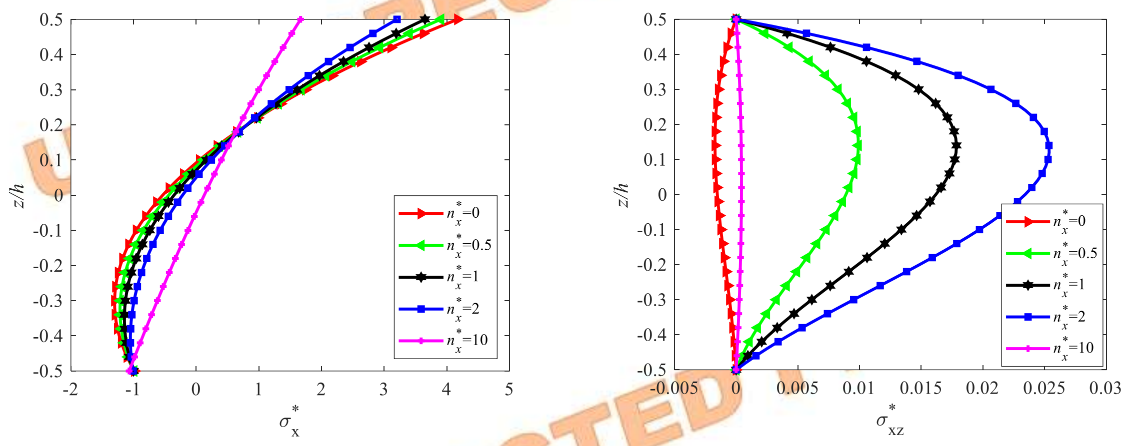

c) Normal stress $\sigma_x^*(z)$ d) Shear stress $\sigma_{xz}^*(z)$ at $x = L/2$

Fig. 9. Effect of the parameter n_x on the nonlinear static response of CS 2DFG-McrBs under UL (Input parameter: $\bar{Q} = 300$; $L = 20h$; $n_z = 1$; $K_W = K_G = 75$; $h^* = 3$)

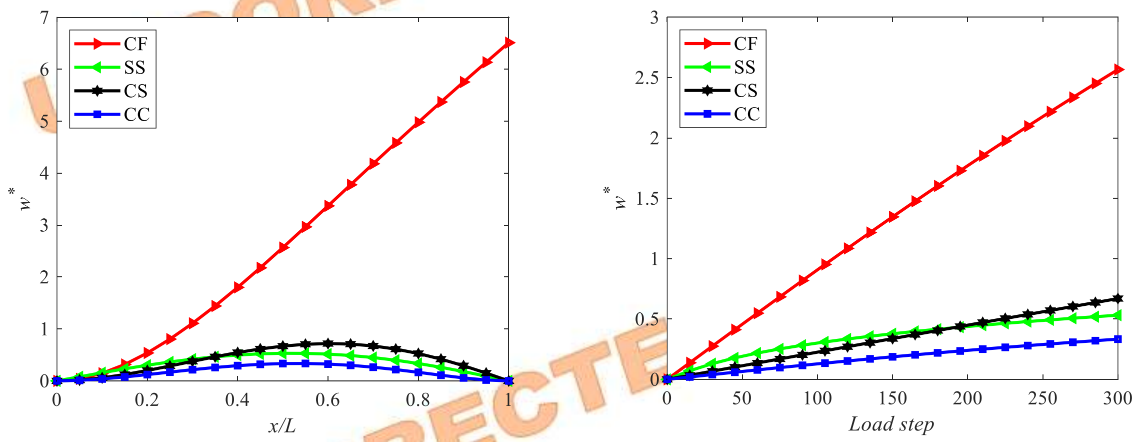

a) The displacement field b) Displacement by load step

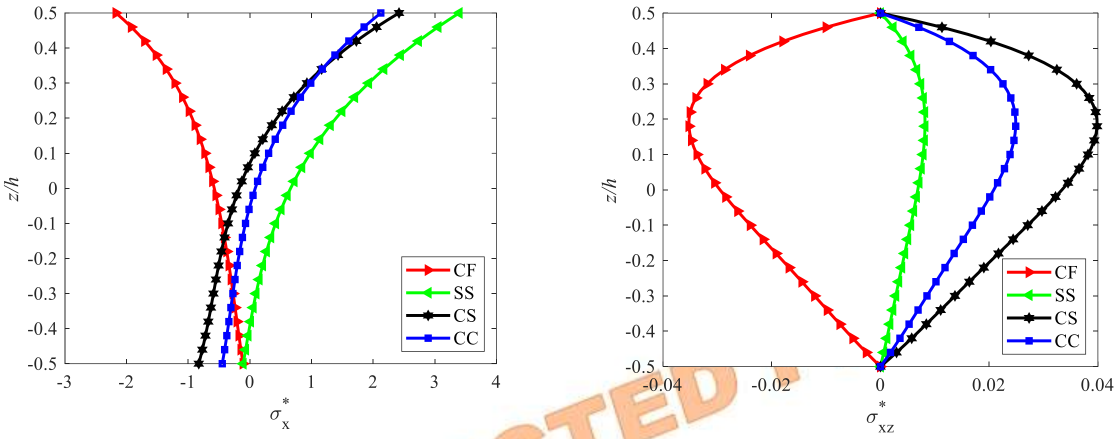

c) Normal stress $\sigma_x^*(z)$ d) Shear stress $\sigma_{xz}^*(z)$ at $x = L/2$

Fig. 10. Effect of BCs on the nonlinear static response of 2DFG-McrBs under UL
(Input parameter: $\bar{Q} = 300; L = 20h; n_x = n_z = 2; K_W = K_G = 25; h^* = 1$)

6. Conclusions

This study presents a finite element framework for analyzing the nonlinear static response of 2DFG-McrBs under various loads while resting on an EF. The influence of microstructural size effects on the nonlinear response is captured using the MCST. Geometrical nonlinearity due to mid-plane stretching of the beam is modeled based on the von Kármán assumption. The resulting discretized nonlinear equilibrium equations are solved using the Newton-Raphson iterative method. The reliability and accuracy of the proposed solution methods are validated by comparing the obtained results with previously published data. Furthermore, the effects of geometric parameters, material properties, four different loads, and BCs on the static nonlinear response of 2DFG-McrBs are thoroughly examined.

Based on the obtained results, for all the load cases and boundary conditions, several key conclusions are drawn as follows:

- The length-scale parameters contribute to increasing the rigidity of 2DFG-McrBs compared to macrobeams.
- EFs play a crucial role in the mechanical response of 2DFG-McrBs. They enhance the beam stiffness, leading to a reduction in displacement. Additionally, the shear layer provides better support than the spring layer.
- As the power-law index increases, the McrB stiffness decreases. Consequently, the displacement of 2DFG-McrBs increases, as expected.
- The proposed algorithm and computational program can be applied to analyze other microstructures with complex geometries embedded in multi-physical environments. This serves as a powerful tool for testing, designing, manufacturing, and optimizing microstructures.

In addition, the developed methodology demonstrates clear advantages in terms of flexibility, accuracy, and computational efficiency. By incorporating microstructural size effects and geometric nonlinearity within a finite element framework, the approach offers a reliable and versatile tool for analyzing microscale structures under realistic loading and boundary conditions. The model's capability to adapt to various design scenarios ensures its potential application in advanced MEMS/NEMS devices and microstructural optimization tasks.

Nomenclature

FG	Functionally graded material
2DFG	Bi-directional functionally graded material
McrB	Microbeam
SGET	Strain gradient elasticity theory
MCST	Modified couple stress theory
FEM	Finite element method
DQM	Differential quadrature method
RBT	Refined beam theory
TBT	Timoshenko beam theory
EBBT	Euler–Bernoulli beam theory
MEMS	Microelectromechanical systems
NEMS	Nanoelectromechanical systems
BC	Boundary condition
DOF	Degree of freedom
EF	Elastic foundation

Funding Statement

This research did not receive any specific grant from funding agencies in the public, commercial, or not-for-profit sectors.

Conflicts of Interest

The author declares that there is no conflict of interest regarding the publication of this article.

References

[1] Younis, M.I., 2011. *MEMS linear and nonlinear statics and dynamics*. Springer Science & Business Media.

[2] Choi, B. & Lovell, E.G., 1997. Improved analysis of mcrbs under mechanical and electrostatic loads. *Journal of Micromechanics and Microengineering, 7* (1).

[3] Chaterjee, S. & Pohit, G., 2009. A large deflection model for the pull-in analysis of electrostatically actuated microcantilever beams. *Journal of Sound and Vibration, 322* (4-5), pp.969–986.

[4] Abdel-Rahman, E.M. & Nayfeh, A.H., 2003. Secondary resonances of electrically actuated resonant microsensors. *Journal of Micromechanics and Microengineering, 13* (3).

[5] Kahrobaiyan, M.H., Asghari, M., Rahaeifard, M. & Ahmadian, M.T., 2011. A nonlinear strain gradient beam formulation. *International Journal of Engineering Science, 49* (11), pp.1256–1267.

[6] Lam, D.C.C., Yang, F., Chong, A.C.M., Wang, J. & Tong, P., 2003. Experiments and theory in strain gradient elasticity. *Journal of the Mechanics and Physics of Solids, 51* (8), pp.1477–1508.

[7] Yang, F.a.C.M., Chong, A.C.M., Lam, D.C.C. & Tong, P., 2002. Couple stress based strain gradient theory for elasticity. *International Journal of Solids and Structures, 39* (10), pp.2731–2743.

[8] Mohammadi, H. & Mahzoon, M., 2013. Thermal effects on postbuckling of nonlinear mcrbs based on the modified strain gradient theory. *Composite Structures, 106*, pp.764–776.

[9] Xia, W., Wang, L. & Yin, L., 2010. Nonlinear non-classical microscale beams: Static bending, postbuckling and free vibration. *International Journal of Engineering Science, 48* (12), pp.2044–2053.

[10] Asghari, M., Kahrobaiyan, M.H. & Ahmadian, M.T., 2010. A nonlinear timoshenko beam formulation based on the modified couple stress theory. *International Journal of Engineering Science, 48* (12), pp.1749–1761.

[11] Pham, Q.-H., Tran, V.K., Tran, T.T., Nguyen, P.-C. & Malekzadeh, P., 2022. Dynamic instability of magnetically embedded functionally graded porous nanobeams using the strain gradient theory. *Alexandria Engineering Journal, 61* (12), pp.10025-10044.

[12] Akgoz, B. & Civalek, O., 2013. Buckling analysis of functionally graded mcrbs based on the strain gradient theory. *Acta Mechanica, 224* (9), pp.2185–2201.

[13] Ramezani, S., 2012. A micro scale geometrically non-linear timoshenko beam model based on strain gradient elasticity theory. *International Journal of Non-Linear Mechanics, 47* (8), pp.863–873.

[14] Ansari, R., Shojaei, M.F. & Gholami, R., 2016. Size-dependent nonlinear mechanical behavior of third-order shear deformable functionally graded mcrbs using the variational differential quadrature method. *Composite Structures, 136*, pp.669–683.

[15] Wang, Y.G., Lin, W.H. & Liu, N., 2015. Nonlinear bending and post-buckling of extensible microscale beams based on modified couple stress theory. *Applied Mathematical Modelling, 39* (1), pp.117–127.

[16] Belabed, Z., Tounsi, A., Bousahla, A.A., Tounsi, A. & Yaylacı, M., 2024. Accurate free and forced vibration behavior prediction of functionally graded sandwich beams with variable cross-section: A finite element assessment. *Mechanics Based Design of Structures and Machines, 52* (11), pp.9144-9177.

[17] Belabed, Z., Bousahla, A.A. & Tounsi, A., 2024. Vibrational and elastic stability responses of functionally graded carbon nanotube reinforced nanocomposite beams via a new quasi-3d finite element model. *Computers and Concrete, 34* (5), pp.625-648.

[18] Belabed, Z., Tounsi, A., Bousahla, A., Tounsi, A., Khedher, K. & Salem, M. Mechanical behavior analysis of fg-cntrc porous beams resting on winkler and pasternak elastic foundations: A finite element approach. Comput. Concrete 34 (4), 447–476 (2024).

[19] Belabed, Z., Tounsi, A., Bousahla, A.A., Tounsi, A., Bourada, M. & Al-Osta, M.A., 2024. Free vibration analysis of bi-directional functionally graded beams using a simple and efficient finite element model. *Structural Engineering and Mechanics, An Int'l Journal, 90* (3), pp.233-252.

[20] Belabed, Z., Tounsi, A., Al-Osta, M.A., Tounsi, A. & Minh, H.-L., 2024. On the elastic stability and free vibration responses of functionally graded porous beams resting on winkler-pasternak foundations via finite element computation. *Geomechanics and Engineering, 36* (2), pp.183-204.

[21] Meftah, S.A., Aldosari, S.M., Tounsi, A., Cuong-Le, T., Khedher, K.M. & Alluqmani, A.E., 2024. Simplified homogenization technique for nonlinear finite element analysis of in-plane loaded masonry walls. *Engineering Structures, 306*, pp.117822.

[22] Tounsi, A., Belabed, Z., Bounouara, F., Balubaid, M., Mahmoud, S., Bousahla, A.A. & Tounsi, A., 2024. A finite element approach for forced dynamical responses of porous fg nanocomposite beams resting on viscoelastic foundations. *International Journal of Structural Stability and Dynamics*, pp.2650078.

[23] Benmesssaoud, M. & Nasreddine, M.M., 2019. Optimization of mems capacitive accelerometer. *Microsystem Technologies*.

[24] Fei, J. & Ding, H., 2017. System dynamics and adaptive control for mems gyroscope sensor. *Applied Industrial Robotics Systems*.

[25] Russo, C., Mocera, F. & Somà, A., 2021. Mems sensors for sport engineer applications. pp.12056.

[26] Şimşek, M., Kocatürk, T. & Akbaş, Ş.D., 2013. Static bending of a functionally graded microbeam timoshenko beam model based on the modified couple stress theory. *Composite Structures, 95*, pp.740–748.

[27] Thai, H.T., Vo, P., Nguyen, T.K. & Lee, J., 2013. Size-dependent behavior of functionally graded sandwich microbeams based on the modified couple stress theory. *Composite Structures, 95*, pp.340–349.

[28] Dehrouyeh-Semnani, A.M., Mostafaei, H. & Nikkhah-Bahrami, M., 2016. Free flexural vibration of geometrically imperfect functionally graded microbeam based on the modified couple stress theory. *Journal of Engineering Science*, pp.56–79.

[29] Sheikholeslami, S.A., Aghdam, M.M., Zappino, E. & Carrera, E., 2017. Application of refined beam theories to the coupled-field analysis of magnetostrictive microbeams. *Composites Part B: Engineering, 115*, pp.1–14.

[30] Akbaş, Ş.D., 2017. Free vibration of cracked functionally graded micro-scale beams based on the modified couple stress theory. *International Journal of Structural Stability and Dynamics, 17*.

[31] Karamanli, A. & Alyodoglu, M., 2020. Vibration of functionally graded and shear deformable porous microplates via the finite element method. *Composite Structures, 237*.

[32] Karamanli, A., Vo, T.P. & Quasi, A., 2021. 3d theory for functionally graded porous microbeams based on the modified strain gradient theory. *Composite Structures, 257*.

[33] Tr, H.H., Lan, Y.U. & Bui, T.Q., 2020. Functionally graded reduced-order timoshenko microbeams: A numerical study using iga and modified couple stress theory. *Composite Structures, 254*.

[34] Attia, M.A. & Mohamed, S.A., 2022. Thermal vibration characteristics of pre/post-buckled bi-directional functionally graded microbeam based on modified couple stress reddy beam theory. *Engineering Computations, 38*, pp.2079–2105.

[35] Shafiei, N., Kazemi, M. & Ghadiri, M., 2016. Nonlinear vibration of axially functionally graded tapered microbeam. *International Journal of Engineering Science, 102*, pp.16–26.

[36] Shafiei, N. & Yarmeni, K., 2017. Nonlinear buckling of functionally graded nano-/micro-scaled porous beams. *Composite Structures, 178*, pp.493–492.

[37] Attia, M.A. & Mohamed, S.A., 2023. Nonlinear thermal buckling and post-buckling analysis of bidirectional functionally graded microbeams based on reddy beam theory. *Engineering Computations, 38*, pp.523–554.

[38] Shenas, A.G., Ziaee, S. & Malekzadeh, P., 2017. Nonlinear vibration analysis of pre-twisted functionally graded microbeams in

thermal environment. *Thin-Walled Structures, 118*, pp.87-104.

[39] Shenas, A.G., Ziaee, S. & Malekzadeh, P., 2021. Nonlinear thermal stability of rotating pre-twisted temperature-dependent fg microblades. *Iranian Journal of Science and Technology, Transactions of Mechanical Engineering, 45*, pp.1-22.

[40] Malekzadeh, P. & Moradi, H., 2024. Large amplitude free vibration of elastically restrained tapered beams resting on non-linear elastic foundation. *Iranian Journal of Science and Technology, Transactions of Mechanical Engineering*, pp.1-12.

[41] Pham, Q.-H., Malekzadeh, P., Tran, V.K. & Nguyen-Thoi, T., 2023. Free vibration analysis of functionally graded porous curved nanobeams on elastic foundation in hygro-thermo-magnetic environment. *Frontiers of Structural and Civil Engineering, 17* (4), pp.584-605.

[42] Nguyen, V.C., Tran, T.T., Sobhy, M., Hoang, N.T. & Pham, Q.H., 2025. The effective finite element method for free and forced vibration analysis of 2d-fgsw plates lying on an elastic foundation. *Mechanical Based Design of Structures and Machines, 53* (2), pp.1329–1350.

[43] Reddy, J.N., 2003. *Mechanics of laminated composite plates and shells: Theory and analysis*. CRC Press.

[44] Thai, H.T., Vo, T.P., Nguyen, T.K. & Lee, J., 2015. Size-dependent behavior of functionally graded sandwich mcrbs based on the modified couple stress theory. *Composite Structures, 123*, pp.337–349.

[45] Karamanlı, A., 2017. Bending behaviour of two directional functionally graded sandwich beams by using a quasi-3d shear deformation theory. *Composite Structures, 174*, pp.70–86.

[46] Dang, N.D., Nguyen, D.K. & Le, C.I., 2024. Size-dependent nonlinear bending of mcrbs based on a third-order shear deformation theory. *Vietnam Journal of Mechanics, 46* (2), pp.119–137.